



Effect of V content on corrosion behavior of high-energy ball milled AA5083

L. Esteves^a, J. Christudasjustus^{a,b}, S.P. O'Brien^{a,b}, C.S. Witharamage^{a,b}, A.A. Darwish^b, G. Walunj^c, P. Stack^a, T. Borkar^c, R.E. Akans^d, R.K. Gupta^{a,b,*}

^a Department of Chemical, Biomolecular and Corrosion Engineering, The University of Akron, Akron, OH, 44325, USA

^b Department of Materials Science and Engineering, North Carolina State University, Raleigh, NC, 27695, USA

^c Department of Mechanical Engineering, Cleveland State University, Cleveland, OH, 44115, USA

^d Concurrent Technologies Corporation, 100 CTC Drive, Johnstown, PA, 15904, USA

ARTICLE INFO

Keywords:

Nanocrystalline alloys
High-energy ball milling
Aluminum-magnesium alloys
Pitting corrosion

ABSTRACT

AA5083 alloys with V additions were produced in the powder form by high-energy ball milling and consolidation by spark plasma sintering and cold compaction. X-ray diffraction and energy dispersive X-ray spectroscopy analysis indicated the formation of supersaturated solid solution and grain refinement below 100 nm. Corrosion behavior was investigated using electrochemical impedance spectroscopy, cyclic potentiodynamic polarization, and immersion corrosion tests followed by surface analysis. The composition of the passive film was obtained via X-ray photoelectron spectroscopy. The corrosion resistance of the AA5083 was significantly improved due to the addition of V and high-energy ball milling.

1. Introduction

Non-heat-treatable 5xxx series alloys, containing Mg and Mn, have been widely used in marine applications due to the high weldability, formability, and corrosion performance [1,2]. Improving corrosion resistance and strength of these alloys would increase their application space. Several processing techniques, able to refine the grain size and intermetallics, have been reported to improve mechanical properties as well as corrosion resistance [3–5]. However, improvement in the corrosion resistance has been incremental [3,6].

Substantial increase in corrosion resistance of Al has been reported by alloying with the corrosion resistant elements like Cr, Mo, W, Nb, Ta, etc. [7–9]. For example, pitting potential of sputter deposited thin film of an Al-W alloy in 0.1 M KCl solution was reported to be ~2545 mV higher than that of pure Al [10]. Solubility of most alloying elements in Al is limited and therefore nonequilibrium processing techniques have been used for the production of Al alloys containing high amount of corrosion resistant alloys in metastable state [3,11]. Ion implantation [12,13] was used to induce high solid solubility of the corrosion resistant elements on the surface and near surface region of the Al alloys. In the later stages, sputter deposition was used to produce thin films of Al alloys which caused high solubility of corrosion resistant elements

[14–16]. These alloys show high corrosion resistance, several orders of magnitude higher than pure Al or any commercial Al alloy. An overview of the corrosion resistant alloys comprising corrosion resistant elements in solid solution and produced by nonequilibrium processing techniques have been reviewed by Esquivel and Gupta [17].

Processing techniques play a critical role in microstructural evolution and attendant corrosion and mechanical properties. Extended solid solubility of selected alloying elements and grain refinement below 100 nm have been reported to cause simultaneous improvement in corrosion resistance and strength of Al [3,7,8]. Esquivel et al. have shown that binary Al alloys, Al-M (M: V, Cr, Mo, Ti, etc.) produced by high-energy ball milling (HEBM), showed combination of high corrosion resistance and strength [9]. Among tested binary alloys, Al-V alloys have shown the best properties and therefore V may be a potential alloying element for the development of ultra-high strength and corrosion resistant Al alloys.

Most studies on enhancing solid solubility of the corrosion resistant alloying elements and therefore corrosion behavior have been focused on binary Al alloys. The influence of these alloying elements on the microstructure and properties of commercial Al alloys is expected to be different than that in binary alloys [17]. Formation of multiple phases and solid solution containing more than one alloying element is

* Corresponding author.

E-mail address: rk Gupta@ncsu.edu (R.K. Gupta).

<https://doi.org/10.1016/j.corsci.2021.109465>

Received 6 October 2020; Received in revised form 18 March 2021; Accepted 6 April 2021

Available online 8 April 2021

0010-938X/© 2021 Elsevier Ltd. All rights reserved.

Table 1

Description of specimens.

Processing for the alloy production	Notation
Commercial AA5083-H116	AA5083-H116
High-energy ball milling of AA5083 powder and subsequent Cold compaction (CC)	CC-HEBM-5083
High-energy ball milling of AA5083 powder with 0.5 wt.% V powder and subsequent Cold compaction (CC)	CC-HEBM-5083–0.5 V
High-energy ball milling of AA5083 powder with 5 wt.% V powder and subsequent Cold compaction (CC)	CC-HEBM-5083–5 V
High-energy ball milling of AA5083 powder and subsequent spark plasma sintering	SPS-HEBM-5083
High-energy ball milling of AA5083 powder with 0.5 wt.% V powder and subsequent spark plasma sintering	SPS-HEBM-5083–0.5 V
High-energy ball milling of AA5083 powder with 5 wt.% V powder and subsequent spark plasma sintering	SPS-HEBM-5083–5 V

expected to result in formation of complex passive film and different corrosion behavior. Therefore, high-energy ball milling of commercial Al alloys with addition of corrosion resistant elements (M) and investigating the microstructure and corrosion behavior is of great merit. In this work, microstructure and corrosion behavior of the high energy ball milled AA5083 alloys with V addition have been investigated.

2. Experimental procedures

2.1. Materials

AA5083 powder (Valimet, size – 325 mesh $D_{90} = 39.46 \mu\text{m}$) with varying amounts of V (0.5 and 5 wt.%) was milled in a planetary ball mill for 100 h at 280 rpm. The ball-to-powder weight ratio (BPR) was 16:1 and 1.5 wt.% of stearic acid was added as a process controlling agent to prevent excessive cold welding of the AA5083 particles [18]. The stainless steel jars were loaded with the processed material and sealed inside of the glove box to keep an inert atmosphere (high purity Ar atmosphere with the concentration of O_2 less than 50 ppm to prevent oxidation and/or contamination of the powder). The milling was interrupted for 30 min after every 1 h of milling to avoid overheating. After HEBM, the powders were consolidated using two techniques: 1) cold compaction (CC) with a uniaxial pressure of 3 GPa at room temperature and 2) spark plasma sintering (SPS) at 400 °C under 600 MPa for 5 min. Table 1 shows a description of the alloys and notation used in this work.

The chemical composition of the alloys produced by high-energy ball milling (HEBM) and subsequent SPS was analyzed using inductively coupled plasma – optical emission spectrometry (ICP-OES) and is presented in Table 2.

2.2. Characterization

2.2.1. Scanning electron microscopy (SEM), energy-dispersive X-ray spectroscopy (EDXS), and transmission electron microscope (TEM)

The CC and SPS specimens were ground up to 1200 grit using SiC paper and fine polished up to 0.05 μm diamond suspension followed by ultrasonic cleaning in ethanol for 5 min. The SEM characterization was performed in a Tescan Lyra 3 FIB-FESEM at an acceleration voltage of 20

kV.

ThermoFisher Quanta 3D FEG, a Focused Ion Beam and Scanning Electron Dual-beam Microscope (FIB-SEM), was utilized to prepare electron-transparent lamellae for TEM analysis. First, a 200 nm Platinum cap was deposited on the area of interest using the electron beam to reduce the ion beam damage to the alloy surface. A landing voltage of 30 kV with different beam currents, depending on the milling step, were used for the FIB sample preparation process. The beam current of 10–30 pA was used for viewing the sample during FIB milling, which minimizes the ion beam damage. Current of 1 nA was used to deposit an extra 2.5 μm Pt on top of the 200-nm Pt-cap, previously deposited to further protect the area of interest from ion beam damage during high-current ion beam milling. To hog out the cross-section from the bulk, series of ion beam currents are used starting with 30, 15, and ending with 5 nA. An Omniprobe micromanipulator was used to conduct in-situ lift-out of the cross-section (currently ~ 1–2 μm thick lamella). This lamella is lifted out and placed on a TEM grid to be thinned down using lower ion beam currents and voltage (15 kV and 1–0.5 nA). The polishing process is carried out to further thin down and clean the cross-section from Ga-contamination using 5 kV and 48 pA ion beam. Final polishing step is necessary and often repeated to make sure the FIB lift-out is within electron transparency. Then, the TEM specimen is kept under vacuum until imaged using the TEM.

The thin FIB lamella is investigated using ThermoFisher Talos F200X G2 that is a 200 kV Field Emission Gun Scanning Transmission Electron Microscope (S/TEM). The TEM specimen is loaded into the Talos S/TEM for chemical mapping and subsurface morphology analyses. Bright-field (BF) and dark field (DF) TEM imaging along with selected-area electron diffraction (SAD) are employed to characterize the subsurface of SPS-HEBM-5083–0.5 V. High-angle annular dark-field (HAADF) imaging and SuperX energy dispersive x-ray spectroscopy (EDXS) are used to capture high-resolution, Z-contrast micrographs and conduct chemical mapping of the cross-section, respectively.

2.2.2. X-ray diffraction (XRD)

The CC and SPS specimens were evaluated using the Rigaku SmartLab X-ray diffractometer with $\text{Cu-K}\alpha$ radiation ($\lambda = 0.1541 \text{ nm}$) with a step size of 0.02° at a scanning speed of 1° per minute in the range of from 25° to 85° of 2θ . The grain size was calculated using the Scherrer equation after subtracting the instrumental broadening [3,4].

2.2.3. X-ray photoelectron spectroscopy (XPS)

The samples used for XPS were immersed for 1 h and 7 days in 0.6 M NaCl solution. XPS was carried out using PHI VersaProbe II operating at an ultra-high vacuum pressure $< 10^{-7}$ Pa. Monochromatic Al-K α radiation is used as X-ray source. The photoelectrons were detected at a 45° take-off angle. The survey scan was conducted from 0 to 1100 eV binding energy. The high-resolution spectra were taken to understand the contribution coming from hydroxide/oxide. The spectrometer was calibrated for peak identification by using the adventitious C1s signal at 285.0 eV. The data was analyzed with the help of CASAXPS software using the Shirley background.

2.2.4. Hardness test

Vickers hardness was measured using a Wilson hardness tester under

Table 2

Chemical composition of AA5083 alloys in weight percentage determined by ICP-OES.

Alloy Element	Al	Mg	Mn	Fe	Si	Cr	Cu	Ti	V
*AA5083-H116 [12]	Bal.	4.0–4.9	0.40–1.0	0.40	0.40	0.05–0.25	0.10	0.15	<0.001
AA5083-H116	Bal.	4.31	0.85	0.178	0.044	0.078	0.038	0.018	<0.001
HEBM-5083	Bal.	4.08	0.600	0.304	0.128	0.109	0.070	0.022	<0.001
HEBM-5083–0.5 V	Bal.	3.92	0.594	0.576	0.144	0.141	0.068	0.021	0.484
HEBM-5083–5 V	Bal.	3.74	0.558	0.426	0.132	0.119	0.064	0.021	4.77

* Nominal composition of AA5083 is also added for comparison.

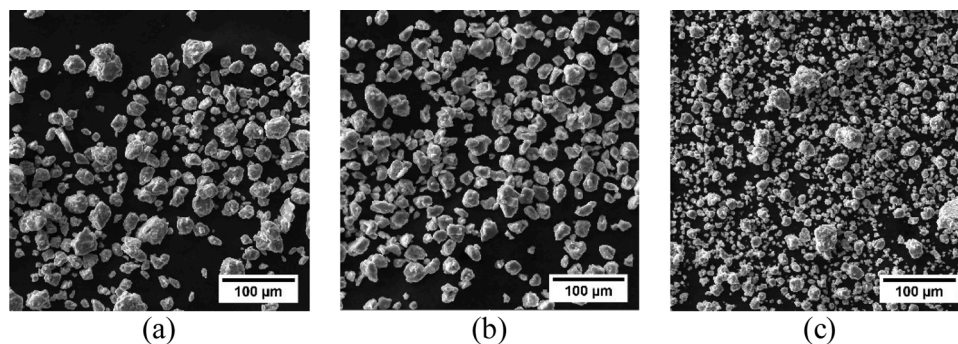


Fig. 1. SE images for the powders of a) HEBM-5083, b) HEBM-5083-0.5 V and c) HEBM-5083-5 V.

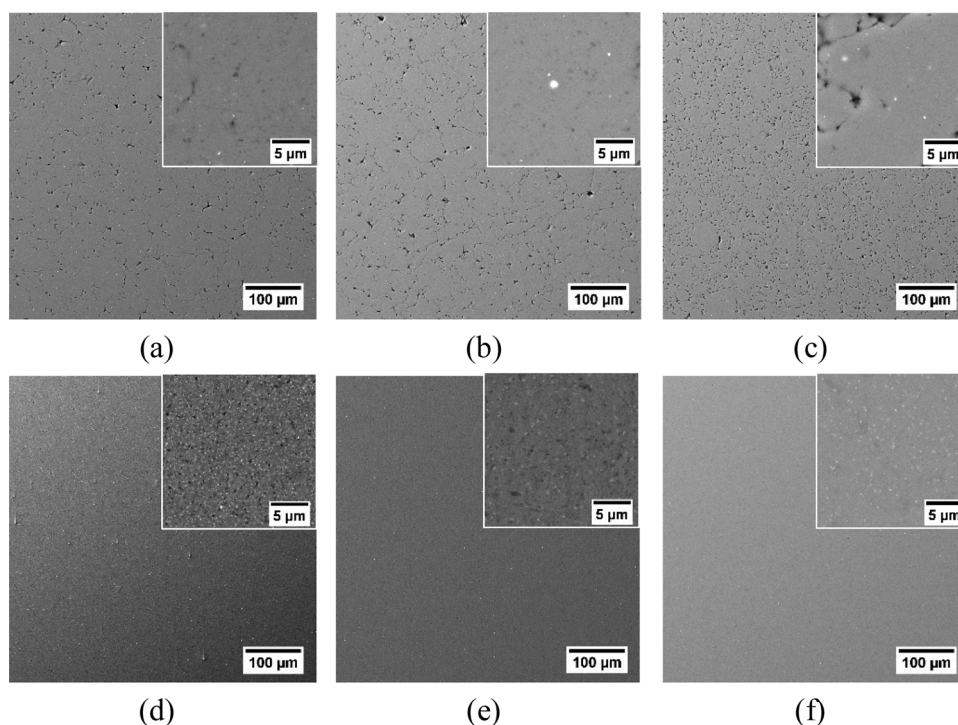


Fig. 2. BSE images for (a) CC-HEBM-5083, (b) CC-HEBM-5083-0.5 V and (c) CC-HEBM-5083-5 V, (d) SPS-HEBM-5083, (e) SPS-HEBM-5083-0.5 V and (f) SPS-HEBM-5083-5 V. Corresponding high magnification images are shown in the inset.

the applied load of 50 g and the dwelling time of 10 s. Ten measurements were taken from each sample to ensure a representative result.

2.2.5. Electrochemical tests

Electrochemical impedance spectroscopy (EIS) and cyclic potentiodynamic polarization (CPP) were performed in 0.6 M NaCl using a conventional flat cell. The specimens were embedded in epoxy resin then an electrical connection was made by copper tape on the back. Specimens were ground to 1200 grit SiC abrasive papers and cleaned with distilled water and ultrasonic cleaning in ethanol and dried with compressed air. Before each experiment, the interface between the sample and epoxy was sealed by epoxy resin (Araldite) at least 12 h before testing to avoid crevice and stored in a desiccator.

A Biologic VMP-300 potentiostat under the control of EC-lab software was used for the electrochemical tests. The tests were carried out in a conventional three-electrode cell. The working electrodes were the aluminum alloys. A platinum mesh as a counter electrode and the reference electrode was a saturated calomel electrode (SCE). The open circuit potential (OCP) was measured for 0.5 h until its stabilization. Then, EIS measurement was performed at stabilized OCP in the

frequency range of 100 kHz to 10 mHz. The CPP curves were obtained at a scan rate of 1 mV/s from 0.1 V_{SCE} below stabilized OCP after 15 min at OCP until the current density reached 1 mA/cm² at which point the scanning direction was then reversed. At least, three sets of measurements were carried out to ensure reproducibility. Exposed surfaces were inspected using optical microscopy (OM). Pit morphology was evaluated by SEM after PDP.

3. Results and discussion

3.1. Characterization

3.1.1. Scanning electron microscopy (SEM), energy-dispersive X-ray spectroscopy (EDXS), and transmission electron microscope (TEM)

Fig. 1 shows the SEM images of the HEBM-5083, HEBM-5083-0.5 V, and HEBM-5083-5 V powders. The V addition affected the particle size and morphology of the high energy ball milled powders. Increasing V content resulted in finer particles which is consistent with the reported influence of the increasing solute content on the particle size after HEBM [3,8,19–21]. Addition of the solute has been reported to enhance the

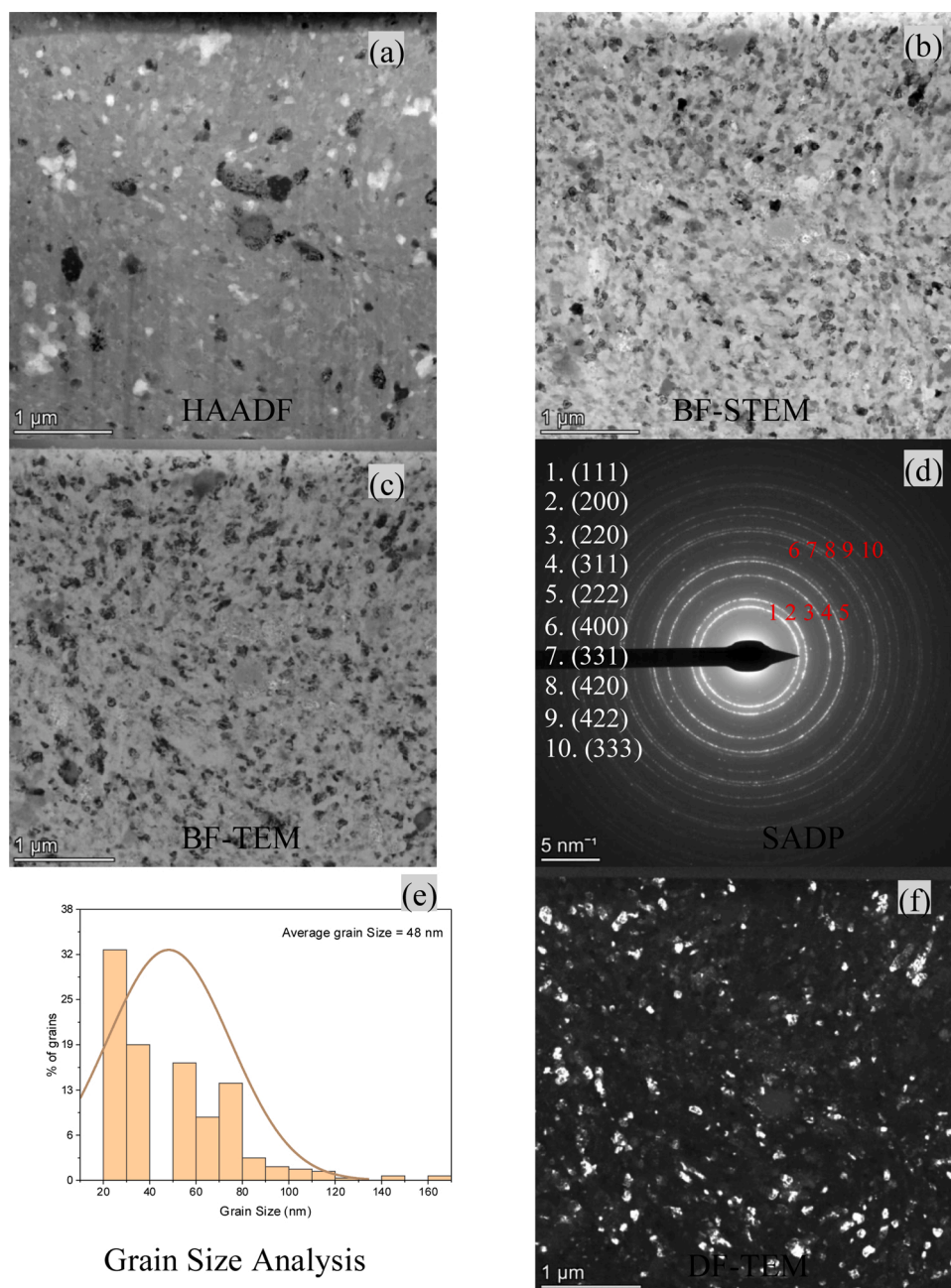


Fig. 3. S/TEM micrographs of SPS-HEBM-5083-0.5 V. (a) HAADF image shows bright and dark phases. (b) BF-STEM image illustrates refined grains of the matrix as confirmed by SADP in (d). BF/DF-TEM images (c and f, respectively) confirms the ultrafine grains of the matrix. (e) shows grain size distribution within the DF-TEM micrograph (f).

work hardening and suppress any recovery which results in refinement of particles as well as grains [19–21].

High-energy ball milled powder was consolidated using cold compaction (CC) and spark plasma sintering (SPS) processes. Annotation for each alloy is given in Table 1. Backscatter electron (BSE) images of the cold compacted and spark plasma sintered alloys are shown in Fig. 2. The cold compacted alloys clearly show presence of pores and their number and size increase with increasing V content. The high-magnification images as shown in the inset revealed uniform distribution of V in these alloys without formation of any coarse phases (Fig. 2a–c). EDXS analysis performed on bright particles revealed the presence of Fe and Cr primarily attributed to the abrasion of milling media during the high-energy ball milling. An EDXS area scan of the bright phase is presented in Fig. S1 (supplementary data) which shows

presence of both Fe and Cr.

Spark plasma sintering was capable of removing pores and improving the overall densification of the alloys (Fig. 2d–f) [3]. Low magnification images clearly showed a more uniform microstructure without any pores, and EDXS analysis confirmed that added V was uniformly distributed in the matrix. High magnification images revealed presence of fine phases (appearing dark) in SPS-HEBM-5083 (Fig. 2d). V addition suppressed the formation of dark phases (Fig. 2e) and addition of 5 wt.% eliminated formation of dark phases. However, a new phase appearing bright was formed due to addition of 5 wt.% V (Fig. 2f).

Fig. 3 shows S/TEM images of the SPS-HEBM-5083-0.5 V. The HAADF image shows bright and dark phases precipitated within the alloy (Fig. 3a). Bright field (BF-STEM) image reveals presence of fine grains in the matrix, which was also confirmed by the selected area

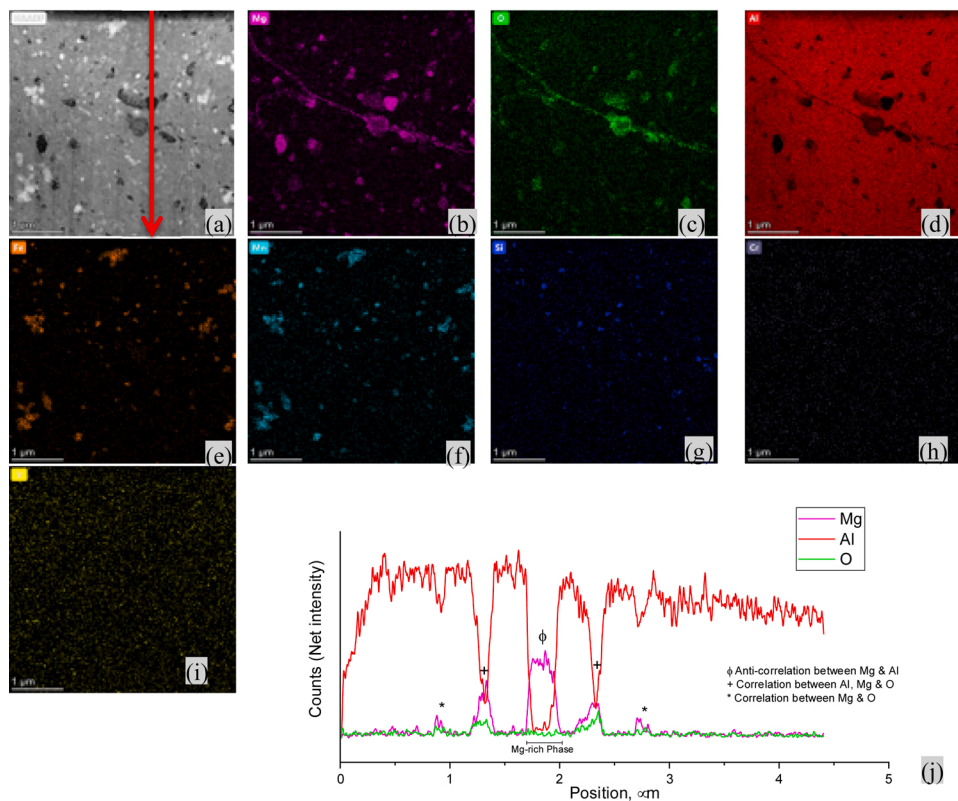


Fig. 4. EDXS-STEM of the SPS-HEBM-5083-0.5 V. (a) HAADF image of the cross-section with a yellow line across the subsurface to indicate the position of the EDS line scan as shown in (j). Super-X EDXS maps shown in (b)-(i) illustrate the presence of mainly two phases, dark (Mg-rich) and bright (Mn-Fe rich) phases, in addition to small traces of Al-Mg-O rich phase. (j) EDXS line-scan along the yellow line in (a), suggesting the existence of Mg-rich and traces of Mg-Al-O rich phases (For interpretation of the references to colour in this figure legend, the reader is referred to the web version of this article).

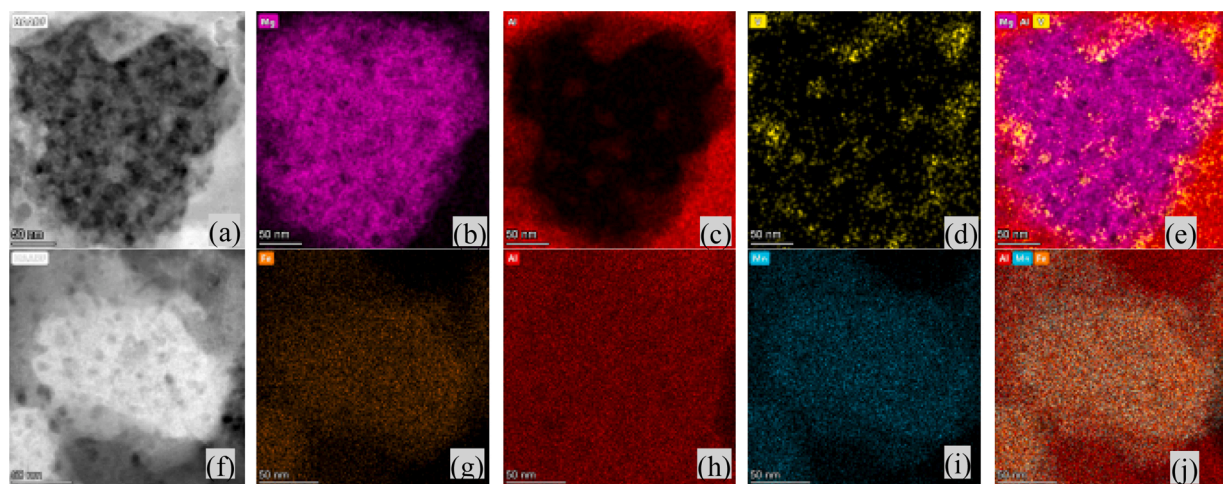


Fig. 5. (a)-(e) HAADF-STEM and EDXS maps of the dark phase in SPS-HEBM-5083-0.5 V, confirming Mg-rich phase with traces of Al and V as shown by EDS maps in (b), (c), and (d). (e) shows superimposed EDS maps of the dark phase. Similarly, (f)-(j) shows the STEM-EDS of the bright phase, suggesting that it is Fe-Mn-Al-rich phase.

diffraction pattern (Fig. 3d). The SADP was compared against Powder Diffraction File™ (PDF®) Databases (PDF Card -00-004-0787_Al) and it was confirmed to belong to FCC-Al with approximate lattice parameter of $4.06814 \pm 0.0058 \text{ \AA}$ [22]. BF/DF-TEM images of the subsurface as shown in (3c) and (3f) confirms the ultrafine grain nature of the matrix. Using ImageJ software [23] for image analysis the grain size was determined to be $48 (\pm 25.5) \text{ nm}$ and grain size distribution is presented in Fig. 3e.

Fig. 4 shows EDXS-STEM image of the SPS-HEBM-5083-0.5 V, where (a) HAADF image of the cross-section with a yellow line across the subsurface to indicate the position of the EDXS line scan analysis (shown in panel j). Super-X EDS maps shown in (b)-(i) illustrate the presence of

mainly two phases, dark (Mg-rich) and bright (Mn-Fe) phases. These phases can also be seen in SEM images as presented in Fig. 2e. Fig. 4(j) shows EDXS line-scan along the yellow line in (Fig. 4a), suggesting the existence of Mg-rich as well as fine Mg-Al-O rich particles. Oxygen may be incorporated either during the sintering or ball milling process. High-energy ball milling is a non-equilibrium processing technique where the possibility of the incorporation of oxygen or other gases into the alloy cannot be overruled. Oxygen may be incorporated during the milling and oxides would form during SPS. Incorporation of oxygen into the Al is reported by several authors [24–26]. The EDXS analysis suggests no correlation between Cr and Fe area maps; which suggests that Fe is precipitated from the matrix not from the milling media. All the

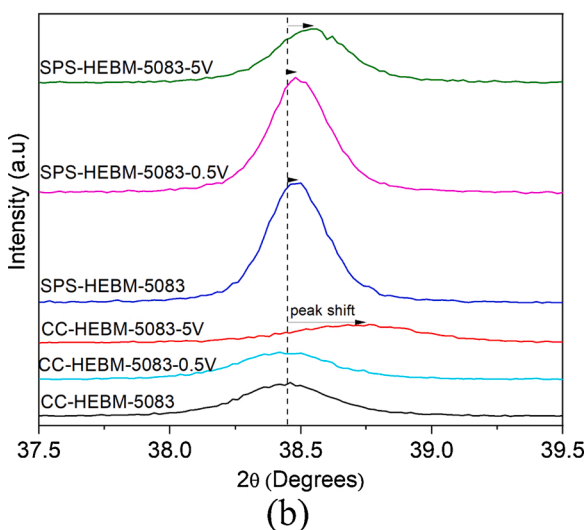
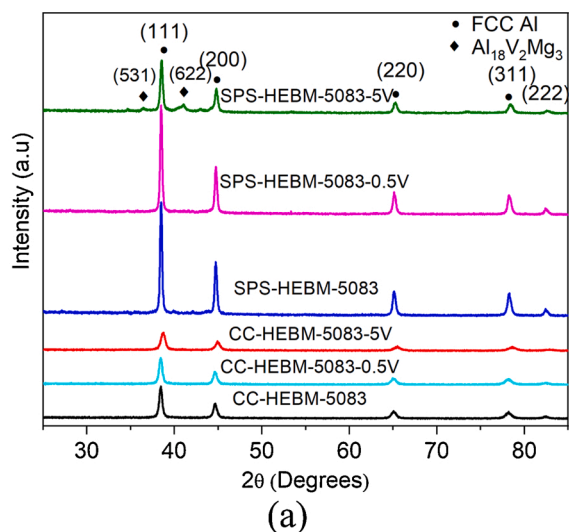


Fig. 6. XRD diffractograms of HEBM-5083, HEBM-5083-0.5 V and HEBM-5083-5 V by CC and SPS consolidation. (a) Full XRD scan, (b) zoomed-in region showing peak shift for Al (111), and (c) zoomed-in of SPS-HEBM-5083-5 V.

bright phases are not formed from the abrasion of the milling media. Also, the correlation between Fe and Mn maps confirms that the white phase is Fe-Mn-rich, while there is correlation between Mg and O maps, which strongly suggests the presence of Mg-O-rich phases in addition to the Mg-rich which appears darker in HAADF micrographs. Fig. 5(a) shows EDXS-STEM of the dark phase in the SPS-HEBM-5083-0.5 V, confirming Mg-rich phase with traces of Al and V as shown by EDXS maps in Fig. 5b–e. The dark phase consists of mainly of Mg with traces of V in the middle and around the phase. Similarly, Fig. 3(f)–(j) shows the EDS of the bright phase, suggesting that it is Fe-Mn-Al-rich phase.

3.1.2. X-ray diffraction (XRD)

X-ray diffraction patterns for the CC-HEBM-5083, CC-HEBM-5083-0.5 V, CC-HEBM-5083-5 V, SPS-HEBM-5083, SPS-HEBM-5083-0.5 V,

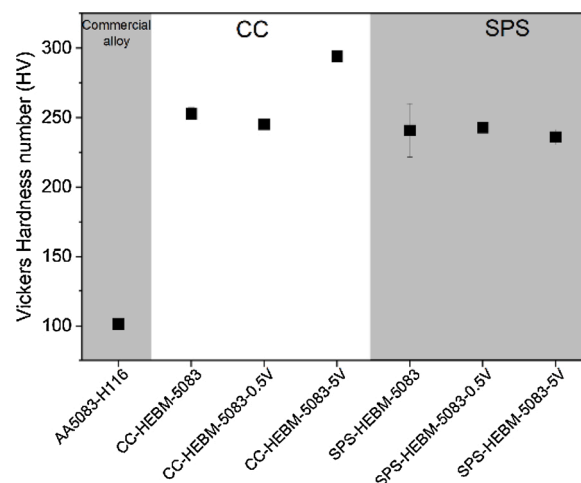


Fig. 7. Vickers hardness of HEBM-5083 and HEBM-5083 containing V consolidated by CC and SPS.

and SPS-HEBM-5083-5 V alloys are shown in Fig. 6. Only FCC Al peaks were observed in all alloys, except for the SPS-HEBM-5083-5 V. The presence of only Al peaks suggests the formation of a homogeneous solid solution without any formation of intermetallics and unalloyed V. The diffractogram for SPS-HEBM-5083-5 V showed the presence of $\text{Al}_{18}\text{V}_2\text{Mg}_3$ intermetallic [27], which is caused by the decomposition of the supersaturated solid solution to the thermodynamically stable microstructure. The formation of $\text{Al}_{18}\text{V}_2\text{Mg}_3$ phase in equilibrium conditions was predicted by software PANDAT™ [28]. It should be noted that the high-energy ball milling is capable of producing microstructures far from equilibrium and, therefore, formation of the thermodynamically stable phases and grain growth is expected due to high temperature exposure during SPS processing [3,21,29–31].

For all the specimens, a zoomed-in region of the XRD peak corresponding to (111) plane of FCC Al showed a peak-shift toward higher 2θ values with the increase in V content (Fig. 6b). The lattice parameter is expected to alter linearly as a function of the amount of alloying elements added in solid solution [21]. In addition, a smaller peak-shift towards higher 2θ values was observed in SPS specimens compared to cold compacted specimens; this can be related to the decomposition of the supersaturated solid solution, as the specimens produced by HEBM are in the metastable state and prone to decomposition to stable phases (FCC Al and intermetallics) when exposed to high temperature during SPS [30]. Solid solubility in binary Al alloys is generally determined by measuring change in the lattice parameter which can be calculated from the shift in peak positions in the X-ray diffraction pattern [32–34]. Calculating precise solid solubility of V in AA5083 was not possible due to the presence of multiple elements.

The grain sizes of cold compacted and spark plasma sintered AA5083 alloys with varying V content are shown in Table 3. The grain size for the cold compacted specimens was smaller as compared to the SPS specimens which can also be observed by the peak broadening (FWHM) and were mainly due to high temperature exposure during SPS processing [3]. Nonetheless, the grain sizes for all SPS processed alloys remained below 100 nm. Addition of V promoted grain refinement in CC alloys and suppressed grain growth during the SPS. Similar behavior was observed in binary Al-V alloys in our previous work which is attributed to the role of V in suppressing the grain growth during SPS and also increasing the grain refinement during HEBM [30]. It should be noted

Table 3

Grain size (determined by XRD analysis using Scherrer equation) of HEBM-5083, HEBM-5083-0.5 V, HEBM-5083-5 V after CC and SPS consolidation.

	CC-HEBM-5083	CC-HEBM-5083–0.5 V	CC-HEBM-5083–5 V	SPS-HEBM-5083	SPS-HEBM-5083–0.5 V	SPS-HEBM-5083–5 V
Grain size (nm)	32.0	29.1	21.3	53.4	53.6	45.2

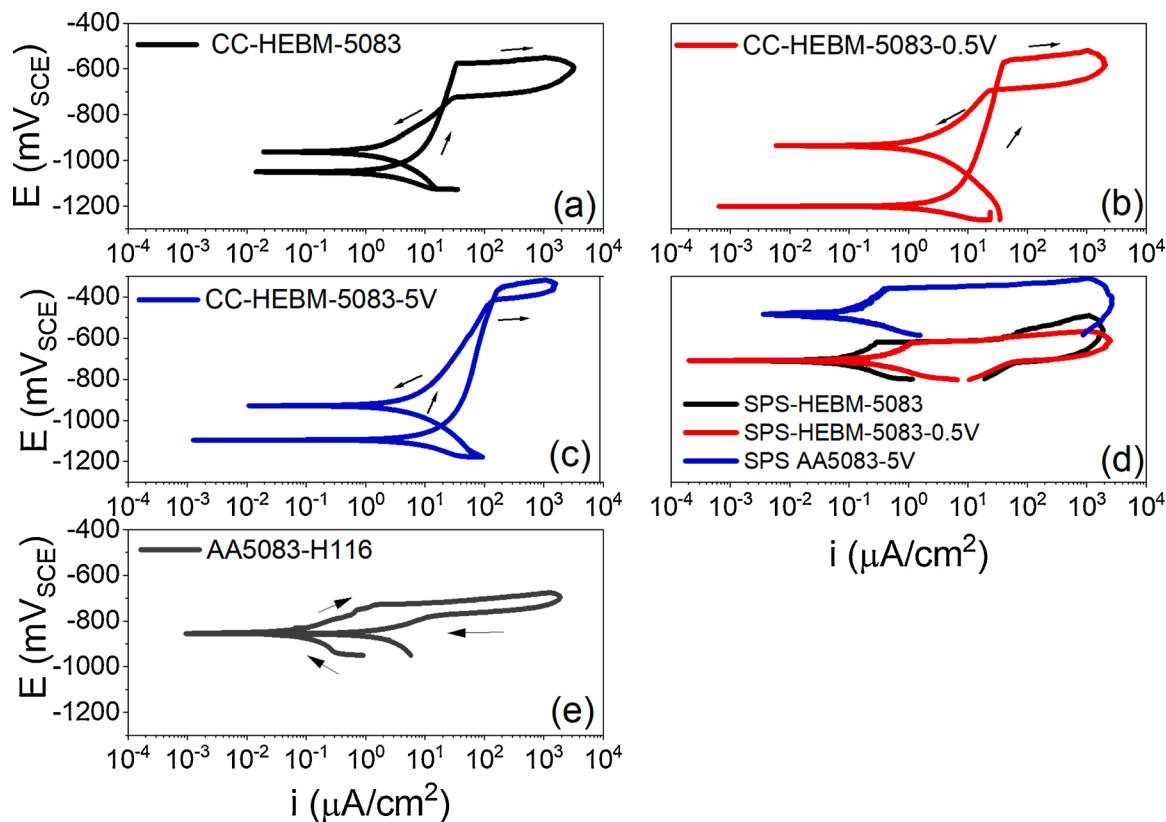


Fig. 8. Representative CPP curves of cold compacted: (a) CC-HEBM-5083, (b) CC-HEBM-5083-0.5 V and (c) CC-HEBM-5083-5 V and (d) SPS specimens (HEBM-5083, HEBM-5083-0.5 V, and HEBM-5083-5 V) in 0.6 M NaCl at room temperature.

Table 4

The average electrochemical parameters and corresponding standard deviation of cold compacted alloys and SPS alloys determined from CPP curves in 0.6 M NaCl at room temperature.

	OCP (mV _{SCE})	E _{pit} (mV _{SCE})	E _{ptp} (mV _{SCE})	E _{prot} (mV _{SCE})	E _{pit} -E _{corr} (mV _{SCE})
CC-HEBM-5083	-1028.9 ± 32.2	-576.3 ± 19.6	-728.2 ± 4.6	-756.6 ± 28.5	499.7
CC-5083-0.5 V	-1229.4 ± 70.0	-549.3 ± 25.2	-	-686.6 ± 4.4	677.3
CC-5083-5 V	-963.5 ± 25.7	-359.6 ± 12.2	-	-433.2 ± 33.9	648.8
SPS HEBM-5083	-781.4 ± 49.2	-685.6 ± 27.7	-776.7 ± 1.2	-	100.3
SPS-HEBM-5083-0.5 V	-801.2 ± 28.8	-653.1 ± 17.1	-762.8 ± 0.8	-	79.6
SPS-HEBM-5083-5 V	-673.6 ± 106.0	-499.3 ± 41.0	-	-	78.6

that average grain size for SPS-AA5083-0.5 V alloy determined using TEM (average grain size =48 nm) is close to that determined using XRD (53.6 nm).

3.1.3. Hardness test

The Vickers hardness as a function of V content is shown in Fig. 7. The CC-HEBM-5083-5 V showed the highest hardness which can be attributed to grain refinement and solid solution strengthening by the extended solubility of V [9,21,35]. Presence of uniformly distributed fine secondary phase particles can also be attributed to the increase in hardness [3]. Esquivel et al. reported a similar value for hardness in a binary Al-5 at.% V (Al-2.7 wt.% V) produced by HEBM [9]. However, the consolidation by SPS for HEBM-5083 containing V showed a

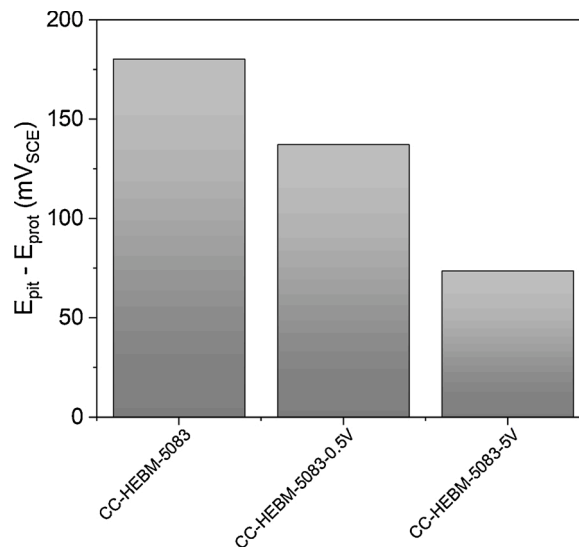


Fig. 9. E_{pit} - E_{prot} values for the CC-HEBM-5083 and CC-HEBM-5083 containing V.

decrease in hardness which could be related to grain growth and decomposition of the solid solution to the thermodynamically phases [30].

3.2. Corrosion tests

Representative cyclic potentiodynamic polarization (CPP) curves for the high-energy ball milled and consolidated alloys tests are shown in Fig. 8. The electrochemical parameters such as stabilized OCP, pitting

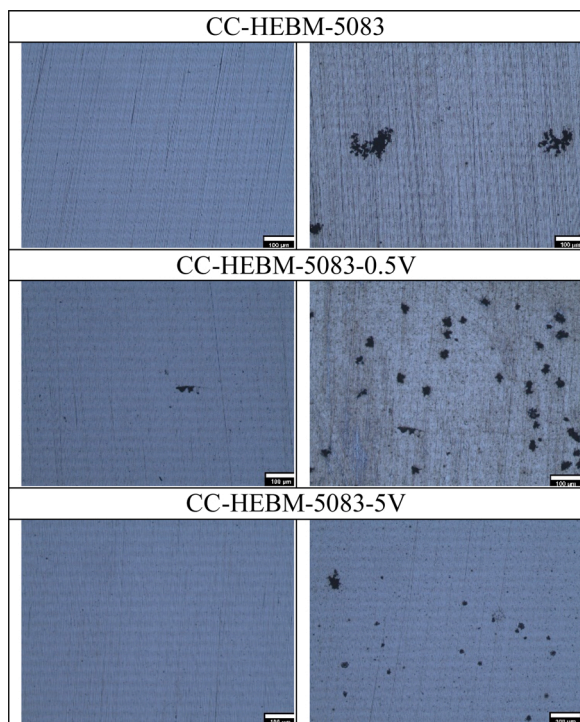


Fig. 10. Optical examination of CC-HEBM-5083, CC-HEBM-5083-0.5 V and CC-HEBM-5083-5 V; left side: before PDP tests and right side: after PDP tests in 0.6 M NaCl.

potential (E_{pit}), pitting current density (i_{pit}), pit transition potential (E_{ptp}), and protection potential (E_{prot}) were determined from the CPP curves and are presented in Table 4. The forward scan showed a passive region with a repassivation potential for all the compositions of the cold compacted specimens, however, the SPS specimens did not exhibit a protection potential (E_{prot}) which was determined as the potential at which the reverse scan intersects the passive region (Fig. 8). Absence of E_{prot} for the SPS specimens indicates that pits propagate with poor repassivation reflecting higher susceptibility to pitting corrosion of the SPS specimens compared to cold compacted specimens. Hysteresis is the variation between $E_{pit} - E_{prot}$ which indicates the difficulty to complete the repassivation of the passive layer due to pit propagation [36]. A comparison of $E_{pit} - E_{prot}$ can be used to evaluate the pitting susceptibility as given in Fig. 9. The results suggest that CC-HEBM-5083-5 V was least susceptible to pitting. Moreover, the cold compacted alloys showed a wider passive window compared to spark plasma sintered alloys (Table 4). These results suggest the localized corrosion resistance can be in the following order: CC-HEBM-5083-5 V > CC-HEBM-5083-0.5 V > CC-HEBM-5083 > SPS-HEBM-5083-5 V > SPS-HEBM-5083-0.5 V > SPS-HEBM-5083. Decrease in the localized corrosion resistance due to the SPS could be attributed to the formation of secondary phases which act as electrochemical heterogenous sites and initiates localized corrosion. As ball milled alloys are supersaturated solid solution with uniform

microstructure, and any activation energy in the form of temperature would cause decomposition to more stable phases [3,8].

Optical microscopy analysis of the surfaces before and after potentiodynamic polarization tests for the cold compacted specimens is shown in Fig. 10. A decrease in the pit size was observed as the V content increased. Furthermore, the SEM micrographs after PDP analyses for the SPS specimens are shown in Fig. 11. The commercial AA5083-H116 showed bigger pits that initiated adjacent to the coarse intermetallics, which are known to act as a cathode promoting anodic dissolution adjacent matrix leading to the formation of pit [37–40].

The EIS data were plotted as Bode plots for SPS HEBM-5083, SPS-HEBM-5083-0.5 V, and SPS-5083-5 V after 15 min of OCP stabilization (Fig. 12a) and after 7 days of immersion in 0.6 M NaCl is shown in Fig. 12b. Nyquist plot with the experimental and fitted data after 7 days is shown in Fig. 12c. The impedance modulus $|Z|$ as a function of frequency. The impedance modulus after both 15 min and 7 days immersion was higher for the SPS-HEBM-5083-5 V, suggesting higher polarization resistance than that of SPS-HEBM-5083 without V. In addition, SPS-HEBM-5083 and SPS-5083-0.5 V showed lower impedance modulus $|Z|$ for 7 days of immersion compared to that for 15 min of OCP stabilization. On the contrary, impedance modulus $|Z|$ for SPS-HEBM-5 V after 7 days immersion was higher than that after 15 min immersion in 0.6 M NaCl. The equivalent electrical circuit (EEC) was based on two-time constants, where the first one was due to the film ($R_{film}-CPE_{film}$) and the second one was due to the metal-oxide interface ($R_{ct}-CPE_{dl}$) elemental loop. R_{ct} represents the charge transfer resistance and CPE_{dl} represents double layer capacitance constant phase element (Fig. 12c). The value of the double layer capacitance (C_{dl}) were calculated by Brug's formula [41–43]. The double layer capacitance (C_{dl}) can be estimated from the constant phase element value (CPE) using the Brug's formula [41–43]. The parameter values obtained are listed in Table 5.

As the constant phase element (CPE) is purely mathematical description without any physical process meaning, the film capacitance (C_{film}) was extracted from the film CPE (CPE_{film}) using the expression developed by Hsu and Mansfeld [43–45]. Then, the film capacitance (C_{film}) can be related to the film thickness (δ_{film}) according to [43]:

$$C_{film} = \frac{\epsilon_0 \epsilon_\gamma}{\delta}$$

C_{film} = capacitance of the film ($F\ cm^{-2}$)

ϵ_0 = electrical permmissivity of vacuum ($8.854 \times 10^{-14}\ F/cm$)

ϵ_γ = dielectric constant of the material (Aluminum oxide) = 11.5 [44]

δ = Film thickness (cm)

The film thickness (δ) corresponding to the film capacitance (C_c) of the studied material are presented in Table 5.

The EIS results after 7 days of immersion in 0.6 M NaCl clearly showed the higher corrosion resistance of SPS-HEBM-5083-5 V. The R_{ct} for SPS-HEBM-5083-5 V was 14 times higher than the SPS-HEBM-5083 and 4 times higher than the commercial AA5083-H116 alloy. Summing up, both electrochemical tests (CPP and EIS) indicated better corrosion behavior of SPS-HEBM-5083-5 V. It should be noted that alloying

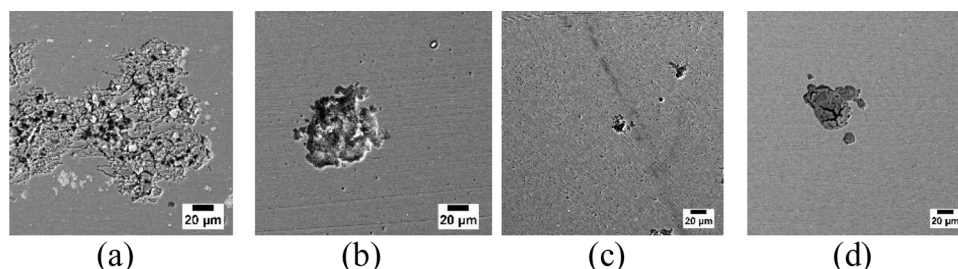


Fig. 11. SEM micrographs after PDP tests of (a) AA5083-H116, (b) SPS-HEBM-5083, (c) SPS-HEBM-5083-0.5 V and (d) SPS-HEBM-5083-5 V in 0.6 M NaCl.

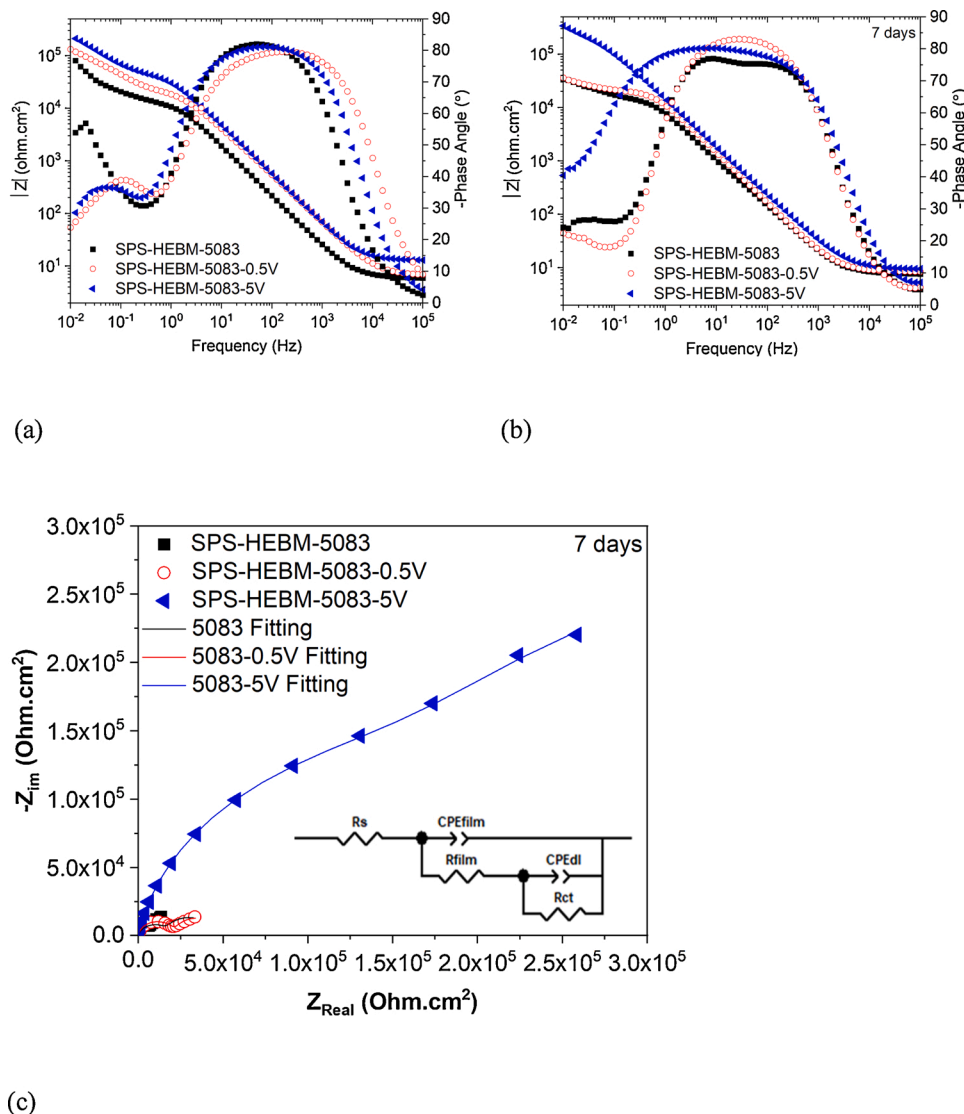


Fig. 12. Bode plots for SPS-HEBM-5083, SPS-HEBM-5083-0.5 V, and SPS-HEBM-5083-5 V alloys (a) after 15 min and (b) after 7 days of OCP stabilization in 0.6 M NaCl, and (c) Nyquist plot after 7 days of immersion.

Table 5

Representative values of the elements of the equivalent electrical circuit of fitting of impedance spectra of AA5083-H116 and SPS-HEBM-5083 specimens after 7 days in 0.6 M NaCl.

Alloy	R_s ($\Omega \cdot \text{cm}^2$)	R_{film} ($\text{k}\Omega \cdot \text{cm}^2$)	CPE_{film} ($\mu\text{Fs}^{n-1} \cdot \text{cm}^2$)	n	CPE_{dl} ($\mu\text{Fs}^{n-1} \cdot \text{cm}^2$)	n	C_{dl} ($\mu\text{F} \cdot \text{cm}^2$)	R_{ct} ($\text{k}\Omega \cdot \text{cm}^2$)	X^2	δ (nm)
AA5083-H116	17	74	6	0.9	212	0.9	61	81	4×10^{-3}	4.0
SPS-HEBM-5083	8	19	23	0.9	394	0.9	130	26	3×10^{-3}	1.1
SPS-HEBM- 5083-0.5 V	9	22	14	0.9	543	0.9	180	27	2×10^{-3}	1.8
SPS-HEBM-5083-5 V	9	320	13	0.9	67	-	67	367	7×10^{-4}	1.4

elements and processing would dictate the microstructure could influence 1) passive film characteristics by changing composition and structure, or 2) influence the repassivation behavior, or 3) combination of the two. Future work comprising of focused microstructure characterization of all the alloys at various processing stages and understanding the electrochemical behavior of individual phases is essential for in-depth theoretical understanding of the corrosion behavior and designing alloys with improved properties.

3.3. Immersion tests: corrosion behavior and surface analysis

Fig. 13 shows the corrosion morphology, before removing the

corrosion products, on AA5083-H116 and V containing SPS-HEBM-5083 alloys after 24 h of immersion in 0.6 M NaCl solution. The SPS-HEBM-5083-5 V showed a uniform distribution of the corrosion product, however, SPS-HEBM-5083 and SPS-HEBM-5083-0.5 V exhibited some cracks in the film. Fig. 14 shows the pit morphology on AA5083-H116 and SPS-HEBM-5083 containing V after 7 days of immersion in 0.6 M NaCl solution and removing the corrosion products. SPS-HEBM-5083 containing V showed least pitting corrosion in comparison to both SPS-HEBM-5083 and AA5083-H116. SPS-HEBM-5083-5 V showed the lowest number of pits. The surface analysis after immersion tests (Figs. 13 and 14) corroborated with the electrochemical results that showed that the specimen containing 5 wt.%V exhibited the highest

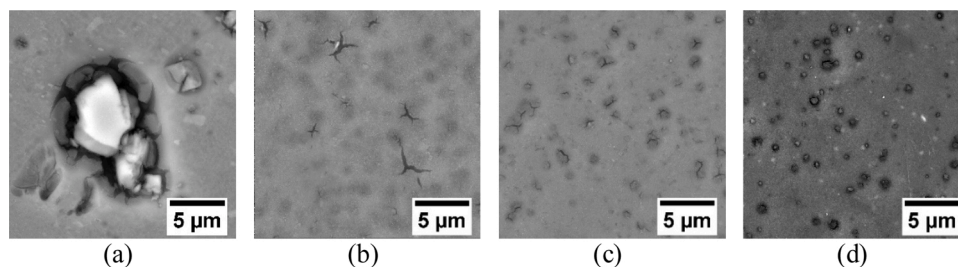


Fig. 13. SEM micrographs after 1 day of immersion in 0.6 M NaCl (a) AA5083-H116, (b) SPS-HEBM-5083, (c) SPS-HEBM-5083-0.5 V, and (d) SPS-HEBM-5083-5 V without removing the corrosion products.

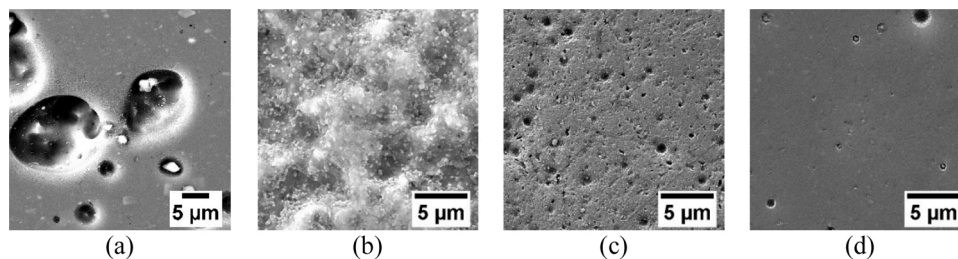


Fig. 14. SE micrographs after 7 days of immersion in 0.6 M (a) AA5083-H116, (b) SPS-HEBM-5083, (c) SPS-HEBM-5083-0.5 V and (d) SPS-HEBM-5083-5 V after removing the corrosion products.

Table 6

The average of pit depth, maximum pit depth and number of pits by IFM: (a) SPS-HEBM, (b) SPS-HEBM-5083-0.5 V, and (c) SPS-HEBM-5083-5 V after 7 days of immersion in 0.6 M NaCl.

7 days immersion in 0.6 M NaCl			
Alloy	Avg. pit depth (µm)	Max. pit depth (µm)	No. of pits
AA5083-H116	7.93	21.2	109
SPS-5083-HEBM	1.85	2.16	42
SPS-5083-HEBM-0.5 V	1.05	1.3	23
SPS-5083-HEBM-5 V	0.3	0.9	11

corrosion resistance.

The infinite focus microscope (IFM) was used to analyze the number and depth of pits. Table 6 shows the pit depth and number after 7 days of immersion in 0.6 M NaCl of AA5083-H116, SPS-HEBM, SPS-HEBM-5083-0.5 V, and SPS-HEBM-5083-5 V. A three-dimensional surface profile is presented in Fig. 15. The AA5083-H116 had the deepest pits compared to the SPS-HEBM specimens, the pits started nearby the coarse intermetallics compared to the SPS-HEBM specimens (Fig. 15). In addition, the SPS-HEBM-5 V showed the lowest average pit depth, lowest maximum pit depth, and the lowest number of pits confirming high pitting corrosion resistance due to the ball milling and alloying with V.

Improved corrosion resistance due to alloying with V could be attributed to change in the chemical composition of the passive film and therefore, x-ray photoelectron spectroscopy (XPS) was performed on the

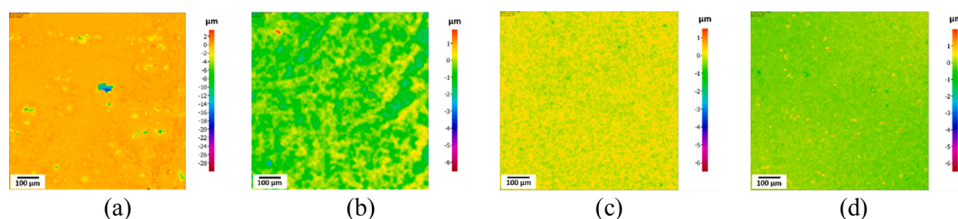


Fig. 15. IFM images of AA503 after immersion for 7 days in 0.6 M NaCl: (a) AA5083-H116 (b) SPS-HEBM-5083, (c) SPS-HEBM-5083-0.5 V and (d) SPS-HEBM-5083-5 V and followed by cleaning with 10 % v/v of HNO₃ to remove the corrosion products.

spark plasma sintered alloys after 1 h and 7 days of immersion in 0.6 M NaCl. Survey scans on the passive film after 1 h and 7 days immersion in 0.6 M NaCl showed the presence of Al and O in all alloys. V was detected only in SPS-HEBM-5083-5 V after both 1 h and 7 days of immersion. High resolution spectra scans, shown in Fig. 16, were performed to reveal the chemical states of the elements. The Al2p spectra consisted of an unoxidized Al (Al⁰) doublet with an energy split of 0.4 eV and oxidized aluminum (Al³⁺) at a binding energy greater than 74 eV [46, 47]. The oxidized aluminum peak was generally referred to as Al³⁺ due to the small binding energy differences between Al oxides and hydroxides [47]. The O1s spectra was deconvoluted into two peaks labeled O-1 and O-2, however, differentiating between oxides and hydroxides is difficult due to the similar Al-O oxide and hydroxide bond lengths [47]. Lastly, the V2p spectra exhibited noisy data, yet a weak peak was observed in the binding energy range of oxidized V, presented in a general oxidized form of Vⁿ⁺ [48]. When comparing the chemical states of Al, a lower atomic concentration of Al⁰, seen in Table 7, was observed for the 7 days immersed specimens compared to the 1 h immersed specimens. The lower Al⁰ content may be due to a thicker passive film, assuming a homogenous film V oxide was not detected in the SPS-HEBM-5083-0.5 V alloys, which may be due to the V content being too low to be detected by the XPS. XPS indicated that a V rich passive film was not formed, however, a small amount of oxidized V was detected in the passive film in SPS-HEBM-5083-5 V alloys.

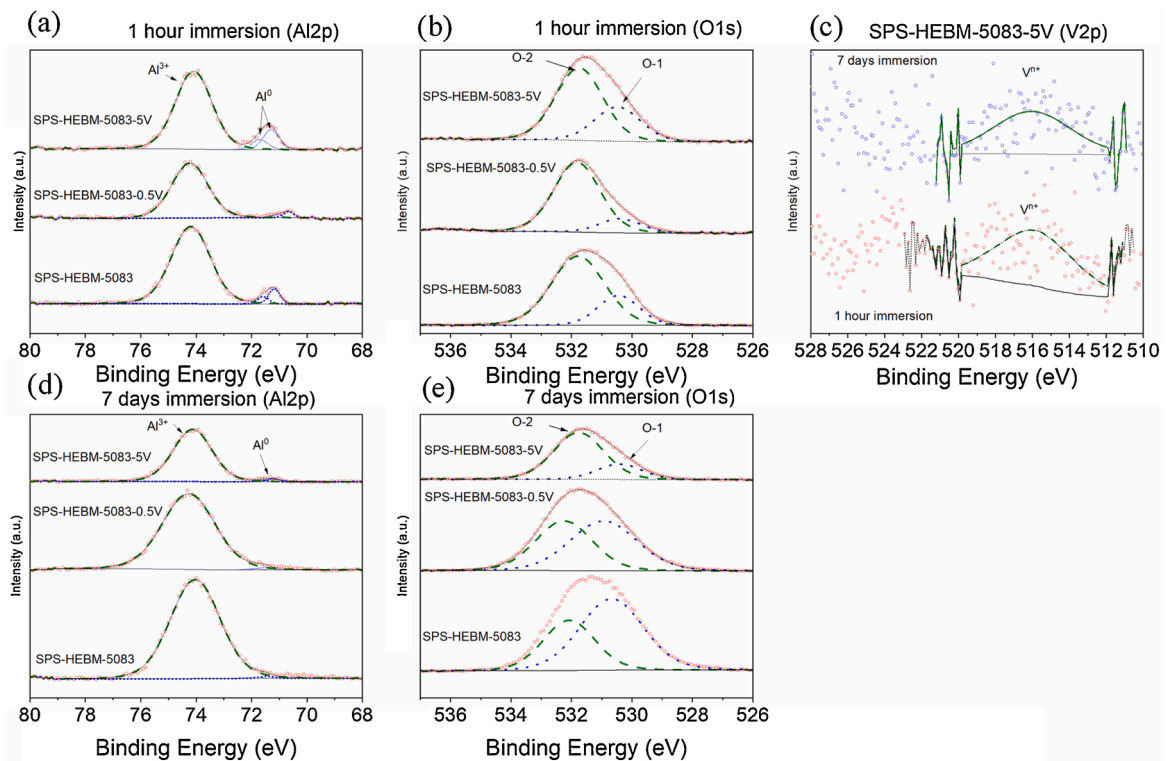


Fig. 16. XPS-spectra of Al2p, O1s, and V2p of the three alloys' (SPS-HEBM-5083, SPS-HEBM-5083-0.5 V, SPS-HEBM-5083-5 V) after (a-c) 1 h immersion and (c-e) 7 days immersion in 0.6 M NaCl.

Table 7

Atomic concentration of SPS-HEBM-5083, SPS-HEBM-5083-0.5 V, SPS-HEBM-5083-5 V after 1 h immersion and 7 days immersion in 0.6 M NaCl.

Immersion time	Alloy	Atomic concentration (%)				
		Al ⁰	Al ³⁺	O ⁻¹	O ⁻²	V ⁿ⁺
1 h	SPS-5083-HEBM	3.28	38.90	14.47	43.35	–
	SPS-5083-HEBM-0.5 V	1.67	34.91	9.96	53.46	–
	SPS-5083-HEBM-5 V	6.15	36.97	17.89	38.72	0.27
7 days	SPS-5083-HEBM	0.35	39.60	38.10	21.95	–
	SPS-5083-HEBM-0.5 V	0.53	37.16	33.71	28.60	–
	SPS-5083-HEBM-5 V	1.00	35.78	14.38	48.56	0.28

3.4. General discussion

The corrosion behavior of the alloy, investigated using CPP and EIS along with the surface characterization after immersion tests, indicated that addition of V to the alloy improved corrosion resistance. Alloys containing 5 wt.%V showed the best corrosion performance. The observed corrosion behavior of the alloys presented herein could be envisioned to be the combined influence of the following microstructural parameters:

- 1) Grain size,
- 2) Solid solubility of the V in the alloy,
- 3) Formation of heterogeneous microstructure (due to SPS) with uniformly distributed V containing intermetallics and matrix with retained V in solid solution form.

The role of the grain size on the corrosion resistance has been

controversial, yet alloys showing passivation in given testing environments have been reported to show improved corrosion performance by grain refinement [3,6,49]. High-energy ball milling has shown improved corrosion resistance of pure Al and AA5083 in our previous work [50]. The addition of V leads to a significant increase in the corrosion resistance which was represented by the high pitting potential and repassivation potential in the cold compacted alloys. Spark plasma sintering resulted in the formation of intermetallic phases and loss of V in solid solution. Corrosion performance of the spark plasma sintered alloys was still high as represented by both electrochemical tests and immersion tests. Such a high corrosion resistance could be attributed to 1) change in the chemical composition of the passive film, or 2) repassivation after breakdown of the passive film. Surface analysis performed by XPS revealed no significant change in the chemical composition due to the alloying with V. Only ~ 0.3 at.% V was detected in alloy containing 5 wt.% V, such a small amount of the V may have a strong influence in improving the corrosion performance by doping effect. For example, doping of oxides with impurities, such as Cr³⁺ addition to Al₂O₃, has been shown to have a strong influence on the characteristics of the oxides [26,51]. Possibility of the occurrence of a similar phenomenon in improving the corrosion resistance of the Al alloys presented herein cannot be overruled. Moreover, role of the incorporation of gases from milling media to the alloy and their impact on corrosion performance needs further research attention. For instance, oxygen content in the sputter deposited thin Al films has been shown to have strong influence on corrosion resistance which could also be the case for high-energy ball milled alloys [26]. Further studies focusing on the influence of V addition on the structure of the passive film, breakdown, and repair of the passive film at various length scales will be required to develop further mechanistic insight. Nonetheless, the corrosion resistance and hardness of the V containing alloys were very high. Further research on improving the properties and studying the detailed mechanical properties, weldability, and corrosion mechanisms would help in improving the properties and engineering applications of these alloys.

4. Conclusions

The effect of V addition on the corrosion of high energy ball milled AA5083 was investigated, and the following are the main conclusions:

- (1) HEBM of AA5083 and V powders lead to the production of alloys with a homogenous microstructure and smaller grain sizes < 100 nm.
- (2) High-energy ball milled alloys were successfully consolidated using SPS process. The SPS sintering is an ideal technique for processing these alloys while retaining their nanocrystalline structure.
- (3) The SPS-HEBM-5 V showed the lowest average pit depth, lowest maximum pit depth, and the lowest number of pits confirming high pitting corrosion resistance due to the ball milling and alloying with V. Overall, AA5083-5 wt.% V alloy exhibited excellent corrosion resistance.
- (4) Hardness of AA5083 alloys has increased due to V addition. The alloys exhibiting high solid solubility of V (and other corrosion resistant alloying elements) and grain size < 100 nm are expected to exhibit high strength and corrosion resistance.

CRediT authorship contribution statement

L. Esteves: Conceptualization, Methodology, Investigation, Formal analysis, Data curation, Writing - original draft, Writing - review & editing. **J. Christudasjustus:** Investigation, Formal analysis, Data curation, Writing - review & editing. **S.P. O'Brien:** Investigation, Formal analysis, Data curation, Writing - review & editing. **C.S. Witharamage:** Investigation, Formal analysis, Data curation, Writing - review & editing. **A.A. Darwish:** Investigation, Formal analysis, Data curation, Writing - review & editing. **G. Walunj:** Investigation. **P. Stack:** Investigation, Formal analysis. **T. Borkar:** Writing - review & editing. **R.E. Akans:** Writing - review & editing. **R.K. Gupta:** Conceptualization, Methodology, Formal analysis, Writing - review & editing, Supervision, Project administration, Funding acquisition.

Declaration of Competing Interest

The authors report no declarations of interest.

Acknowledgments

The financial support from the Concurrent Technologies Corporation, USA (Award 1000004476) with Mr. Robert Mason as technical program manager is highly appreciated. The financial support from the National Science Foundation, USA (Award NSF-CMMI 1760204) under the direction of Dr. Alexis Lewis is highly acknowledged.

Appendix A. Supplementary data

Supplementary material related to this article can be found, in the online version, at doi:<https://doi.org/10.1016/j.corsci.2021.109465>.

References

- [1] M.A. Steiner, S.R. Agnew, Modeling sensitization of Al-Mg alloys via β -phase precipitation kinetics, *Scr. Mater.* 102 (2015) 55–58, <https://doi.org/10.1016/j.scriptamat.2015.02.012>.
- [2] Y.K. Yang, T. Allen, Direct visualization of β phase causing intergranular forms of corrosion in Al-Mg alloys, *Mater. Charact.* 80 (2013) 76–85, <https://doi.org/10.1016/j.matchar.2013.03.014>.
- [3] R.K. Gupta, B.S. Murty, N. Birbilis, *An Overview of High-energy Ball Milled Nanocrystalline Aluminum Alloys*, Springer, 2017, <https://doi.org/10.1007/978-3-319-57031-0>.
- [4] G. Wu, C. Liu, L. Sun, Q. Wang, B. Sun, B. Han, J.J. Kai, J. Luan, C.T. Liu, K. Cao, Y. Lu, L. Cheng, J. Lu, Hierarchical nanostructured aluminum alloy with ultrahigh strength and large plasticity, *Nat. Commun.* 10 (2019) 1–8, <https://doi.org/10.1038/s41467-019-13087-4>.
- [5] F.C. Li, T. Liu, J.Y. Zhang, S. Shuang, Q. Wang, A.D. Wang, J.G. Wang, Y. Yang, Amorphous–nanocrystalline alloys: fabrication, properties, and applications, *Mater. Today Adv.* 4 (2019), <https://doi.org/10.1016/j.mtadv.2019.100027>.
- [6] K.D. Ralston, N. Birbilis, Effect of grain size on corrosion, *Corrosion* 66 (2010) 1–4, <https://doi.org/10.5006/1.3462912>.
- [7] R.K. Gupta, D. Fabijanic, T. Dorin, Y. Qiu, J.T. Wang, N. Birbilis, Simultaneous improvement in the strength and corrosion resistance of Al via high-energy ball milling and Cr alloying, *Mater. Des.* 84 (2015) 270–276, <https://doi.org/10.1016/j.matdes.2015.06.120>.
- [8] R.K. Gupta, D. Fabijanic, R. Zhang, N. Birbilis, Corrosion behaviour and hardness of in situ consolidated nanostructured Al and Al-Cr alloys produced via high-energy ball milling, *Corros. Sci.* 98 (2015) 643–650, <https://doi.org/10.1016/j.corsci.2015.06.011>.
- [9] J. Esquivel, H.A. Murdoch, K.A. Darling, R.K. Gupta, Excellent corrosion resistance and hardness in Al alloys by extended solid solubility and nanocrystalline structure, *Mater. Res. Lett.* 6 (2018) 79–83, <https://doi.org/10.1080/21663831.2017.1396262>.
- [10] B.A. Shaw, G.D. Davis, T.L. Fritz, B.J. Rees, W.C. Moshier, The influence of tungsten alloying additions on the passivity of aluminum, *J. Electrochem. Soc.* 138 (1991) 3288–3295, <https://doi.org/10.1149/1.2085404>.
- [11] T. Dorin, N. Stanford, N. Birbilis, R.K. Gupta, Influence of cooling rate on the microstructure and corrosion behavior of Al-Fe alloys, *Corros. Sci.* 100 (2015) 396, <https://doi.org/10.1016/j.corsci.2015.08.017>.
- [12] E. McCafferty, Effect of ion implantation on the corrosion behavior of iron, stainless steels, and aluminum - a review, *Corrosion* 57 (2001) 1011–1029, <https://doi.org/10.5006/1.3281675>.
- [13] M.V. Zeller, J.A. Kargol, Surface analysis studies on the corrosion resistance of Mo implanted Al alloys, *Appl. Surf. Sci.* 18 (1984) 63–85, <https://doi.org/10.1111/j.1600-0765.1973.tb02172.x>.
- [14] W.C. Moshier, G.D. Davis, J.S. Ahearn, H.F. Hough, Corrosion behavior of aluminum-molybdenum alloys in chloride solutions, *J. Electrochem. Soc.* 134 (1987) 2677–2684, <https://doi.org/10.1149/1.2100271>.
- [15] G.S. Frankel, R.C. Newman, C.V. Jahnes, M.A. Russak, On the pitting resistance of sputter-deposited aluminum alloys, *J. Electrochem. Soc.* 140 (1993) 2192–2197, <https://doi.org/10.1149/1.2220794>.
- [16] P.J. Kelly, R.D. Arnell, Magnetron sputtering: a review of recent developments and applications, *Vacuum* 56 (2000) 159–172, [https://doi.org/10.1016/S0042-207X\(99\)00189-X](https://doi.org/10.1016/S0042-207X(99)00189-X).
- [17] J. Esquivel, R.K. Gupta, Review—corrosion-resistant metastable Al alloys: an overview of corrosion mechanisms, *J. Electrochem. Soc.* 167 (2020) 081504, <https://doi.org/10.1149/1945-7111/ab8a97>.
- [18] L. Lu, Y.F. Zhang, Influence of process control agent on interdiffusion between Al and Mg during mechanical alloying, *J. Alloys Compd.* 290 (1999) 279–283, [https://doi.org/10.1016/S0925-8388\(99\)00221-2](https://doi.org/10.1016/S0925-8388(99)00221-2).
- [19] D.K. Mukhopadhyay, C. Suryanarayana, F.H. (SAM) Froes, Structural evolution in mechanically alloyed Al-Fe powders, *Metall. Mater. Trans. A.* 26 (1995) 1939–1946, <https://doi.org/10.1007/BF02670665>.
- [20] G.J. Fan, W.N. Gao, M.X. Quan, Z.Q. Hu, Preparation and thermal stability of supersaturated nanocrystalline Al-Ti alloys, *Mater. Lett.* 23 (1995) 33–37, [https://doi.org/10.1016/0167-577X\(94\)00266-5](https://doi.org/10.1016/0167-577X(94)00266-5).
- [21] J. Esquivel, R.K. Gupta, Influence of the V content on microstructure and hardness of high-energy ball milled nanocrystalline Al-V alloys, *J. Alloys Compd.* 760 (2018) 63–70, <https://doi.org/10.1016/j.jallcom.2018.05.132>.
- [22] S. Gates-Rector, T. Blanton, The Powder Diffraction File: a quality materials characterization database, *Powder Diffr.* 34 (2019) 352–360, <https://doi.org/10.1017/S0885715619000812>.
- [23] C.A. Schneider, W.S. Rasband, K.W. Eliceiri, NIH Image to ImageJ: 25 years of image analysis, *Nat. Methods* 9 (2012) 671–675, <https://doi.org/10.1038/nmeth.2089>.
- [24] F. Tang, D.S. Gianola, M.P. Moody, K.J. Hemker, J.M. Cairney, Observations of grain boundary impurities in nanocrystalline Al and their influence on microstructural stability and mechanical behaviour, *Acta Mater.* 60 (2012) 1038–1047, <https://doi.org/10.1016/j.actamat.2011.10.061>.
- [25] M.-R. He, S.K. Samudrala, G. Kim, P.J. Felfel, A.J. Breen, J.M. Cairney, D. S. Gianola, Linking stress-driven microstructural evolution in nanocrystalline aluminium with grain boundary doping of oxygen, *Nat. Commun.* 7 (2016), 11225, <https://doi.org/10.1038/ncomms11225>.
- [26] G.S. Frankel, X.-B. Chen, R.K. Gupta, S. Kandasamy, N. Birbilis, Effect of vacuum system base pressure on corrosion resistance of sputtered Al thin films, *J. Electrochem. Soc.* 161 (2014) C195–C200, <https://doi.org/10.1149/2.056404jes>.
- [27] M. Lech-Grega, W. Szymański, M. Gawlik, M. Bigaj, Homogenization of 6xxx alloy ingots with an addition of vanadium, *ICAA13 Pittsburgh*, Springer, Cham, 2012, pp. 1551–1558, https://doi.org/10.1007/978-3-319-48761-8_234.
- [28] L.L.C. CompuTherm, Pandat® Software. Pandat and PanAl Databases, 2020.
- [29] J. Eckert, J.C. Holzer, C.E. Krill, W.L. Johnson, Structural and thermodynamic properties of nanocrystalline fcc metals prepared by mechanical attrition, *J. Mater. Res.* 7 (1992) 1751–1761, <https://doi.org/10.1557/JMR.1992.1751>.
- [30] J. Esquivel, M.G. Wachowiak, S.P. O'Brien, R.K. Gupta, Thermal stability of nanocrystalline Al-5at.%Ni and Al-5at.%V alloys produced by high-energy ball milling, *J. Alloys Compd.* 744 (2018) 651–657, <https://doi.org/10.1016/j.jallcom.2018.02.144>.
- [31] L. Shaw, H. Luo, J. Villegas, D. Miracle, Effects of internal strains on hardness of nanocrystalline Al-Fe-Cr-Ti alloys, *Scr. Mater.* 51 (2004) 449–453, <https://doi.org/10.1016/j.scriptamat.2003.12.033>.

- [32] C. Suryanarayana, Mechanical alloying and milling, *Prog. Mater. Sci.* 46 (2001) 1–184.
- [33] N.W. Denton, A.R. Ashcroft, Vegard's law, *Phys. Rev. A* 43 (1991) 3161–3164, <https://doi.org/10.1002/pssb.19660180251>.
- [34] T. Fujii, Correlation of some physical properties and chemical composition of solid solution, *Am. Mineral.* 45 (1960) 370–382.
- [35] T.J. Rupert, J.C. Trenkle, C.A. Schuh, Enhanced solid solution effects on the strength of nanocrystalline alloys, *Acta Mater.* 59 (2011) 1619–1631, <https://doi.org/10.1016/j.actamat.2010.11.026>.
- [36] M. Trueba, S.P. Trasatti, Study of Al alloy corrosion in neutral NaCl by the pitting scan technique, *Mater. Chem. Phys.* 121 (2010) 523–533, <https://doi.org/10.1016/j.matchemphys.2010.02.022>.
- [37] K.A. Yasakau, M.L. Zheludkevich, S.V. Lamaka, M.G.S. Ferreira, Role of intermetallic phases in localized corrosion of AA5083, *Electrochim. Acta* 52 (2007) 7651–7659, <https://doi.org/10.1016/j.electacta.2006.12.072>.
- [38] N. Birbilis, R.G. Buchheit, Electrochemical characteristics of intermetallic phases in aluminum alloys, *J. Electrochem. Soc.* 152 (2005) B140, <https://doi.org/10.1149/1.1869984>.
- [39] R.K. Gupta, N.L. Sukiman, M.K. Cavanaugh, B.R.W. Hinton, C.R. Hutchinson, N. Birbilis, Metastable pitting characteristics of aluminium alloys measured using current transients during potentiostatic polarisation, *Electrochim. Acta* 66 (2012) 245–254, <https://doi.org/10.1016/j.electacta.2012.01.090>.
- [40] R.K. Gupta, B.R.W. Hinton, N. Birbilis, The effect of chromate on the pitting susceptibility of AA7075-T651 studied using potentiostatic transients, *Corros. Sci.* 82 (2014) 197–207, <https://doi.org/10.1016/j.corsci.2014.01.012>.
- [41] G.J. Brug, A.L.G. van den Eeden, M. Sluyters-Rehbach, J.H. Sluyters, The analysis of electrode impedances complicated by the presence of a constant phase element, *J. Electroanal. Chem.* 176 (1984) 275–295, [https://doi.org/10.1016/S0022-0728\(84\)80324-1](https://doi.org/10.1016/S0022-0728(84)80324-1).
- [42] B. Tribollet, U.P.R. Cnrs, U. Pierre, Analysis of constant phase element, *ECS Meet. Abstr.* 1 (2013), 75252, <https://doi.org/10.1149/ma2013-01/28/1043>.
- [43] B. Hirschorn, M.E. Orazem, B. Tribollet, V. Vivier, I. Frateur, M. Musiani, Determination of effective capacitance and film thickness from constant-phase-element parameters, *Electrochim. Acta* 55 (2010) 6218–6227, <https://doi.org/10.1016/j.electacta.2009.10.065>.
- [44] B. Hirschorn, M.E. Orazem, B. Tribollet, V. Vivier, I. Frateur, M. Musiani, Constant-phase-Element behavior caused by resistivity distributions in films, *J. Electrochem. Soc.* 157 (2010) C458, <https://doi.org/10.1149/1.3499565>.
- [45] C.H. Hsu, F. Mansfeld, Technical note: concerning the conversion of the constant phase element parameter Y 0 into a capacitance, *Corrosion* 57 (2001) 747–748, <https://doi.org/10.5006/1.3280607>.
- [46] G. Greczynski, L. Hultman, X-ray photoelectron spectroscopy: towards reliable binding energy referencing, *Prog. Mater. Sci.* 107 (2020), 100591.
- [47] J.A. Rotole, P.M.A. Sherwood, Valence band x-ray photoelectron spectroscopic studies to distinguish between oxidized aluminum species, *J. Vac. Sci. Technol. A Vacuum Surf. Film* 17 (1999) 1091–1096, <https://doi.org/10.1116/1.581779>.
- [48] E. Hryha, E. Rutqvist, L. Nyborg, Stoichiometric vanadium oxides studied by XPS, *Surf. Interface Anal.* 44 (2012) 1022–1025, <https://doi.org/10.1002/sia.3844>.
- [49] R.K. Gupta, N. Birbilis, The influence of nanocrystalline structure and processing route on corrosion of stainless steel : a review, *Corros. Sci.* (2014), <https://doi.org/10.1016/j.corsci.2014.11.041>.
- [50] L. Esteves, S. Witharamage, J. Christudasjustus, P. Stack, G. Walunj, S. Ryu, T. Borkar, E. Akans, R.K. Gupta, Influence of high-energy ball milling on corrosion behavior of AA5083, *J. Alloys Compd.* (857) (2021), 158268, <https://doi.org/10.1016/j.jallcom.2020.15826>.
- [51] J.P. Buban, K. Matsunaga, J. Chen, N. Shibata, W.Y. Ching, T. Yamamoto, Y. Ikuhara, Grain boundary strengthening in alumina by rare earth impurities, *Science* (80-) 311 (2006) 212–215, <https://doi.org/10.1126/science.1119839>.